Research Square

Preprints are preliminary reports that have not undergone peer review.
They should not be considered conclusive, used to inform clinical practice,
or referenced by the media as validated information.

Multielement absorption-edge complementarity in liquid metal amalgams enables Pb-free, lightweight, and flexible X-ray shielding

Wei Rao

weirao@mail.ipc.ac.cn

Technical Institute of Physics and Chemistry, Chinese Academy of Sciences https://orcid.org/0000-0002-4168-0298

Yunlong Bai

Technical Institute of Physics and Chemistry, Chinese Academy of Sciences

Li Liu

The University of Sydney https://orcid.org/0000-0003-0093-5191

Zhaosen Yuan

School of Science, China University of Geosciences (Beijing) https://orcid.org/0009-0003-9928-6634

Jun Su

Technical Institute of Physics and Chemistry, Chinese Academy of Sciences

Tangzhen Guan

Technical Institute of Physics and Chemistry, Chinese Academy of Sciences

Zhen Zhang

Technical Institute of Physics and Chemistry, Chinese Academy of Sciences

Yujing Liu

School of Information Science and Technology, Beijing Forestry University

Minghui Guo

Chinese Academy of Sciences

Jianbo Tang

Westlake University https://orcid.org/0000-0002-0155-6807

Article

Keywords:

Posted Date: October 6th, 2026

DOI: https://doi.org/10.21203/rs.3.rs-10930041/v1

License: This work is licensed under a Creative Commons Attribution 4.0 International License.
Read Full License

Additional Declarations: There is **NO** Competing Interest.

Abstract

X-ray protection is becoming increasingly important for medical/industrial diagnostics and space exploration. Conventional X-ray shielding materials suffer from bulkiness, rigidity, toxicity and weak absorption windows. Here, we use a ternary Ga-In-Sn liquid alloy as a malleable matrix to disperse up to 27 metallic elements to form a Pb-free, high-shielding-performance, conformable liquid metal amalgam. Due to the presence of 208 superposable resonant absorption edges in the material, it effectively eliminates weak shielding windows across the 1-100 keV energy range, and achieves a 39% increase compared with mass-equivalent Pb. It is able to conform to curved surfaces, withstand prolonged irradiation, and retain shielding performance under 1000% strain. This work offers a transformative route to Pb-free, lightweight, and flexible X-ray shielding materials for improved X-ray safety.

Main Text

X-rays have achieved widespread applications in critical fields such as medical imaging[1], reactor monitoring[2], and industrial radiography[3]. X-ray safety has become a core bottleneck hindering the development of related technologies[4]. Lead (Pb), as the gold standard for X-ray shielding, has long been the most widely adopted material[5]. However, the weak absorption of Pb in the 40–88 keV energy window constitutes a critical limitation, as this region overlaps with the peak photon flux of typical medical X-ray sources (50–150 kVp)[6]. In addition, Pb and Pb-based X-ray shielding materials are known to suffer from biotoxicity, bulkiness, rigidity and radiation-induced cracking[7,8]. To accommodate the fast-growing X-ray technologies and the broadening of the applied X-ray photon energy range[9], the development of Pb-free lightweight shielding materials with no weak absorption window is in high demand for optimal X-ray protection.

When the core-electron binding energy of an X-ray shielding material matches the incident X-ray energy, resonant excitation of its core electrons occurs[10]. The resulting *absorption edge resonance* (AER) effect greatly enhances the X-ray mass attenuation coefficient (Fig. 1a)[11]. For instance, the K-absorption edge resonance of gallium (Ga) occurs at a photon energy of 10.37 keV, and upon reaching it, Ga shows a sharp increase in its mass attenuation coefficient from 31 cm^2/g to 221.4 cm^2/g (Supplementary Fig. 1a). Since changing the atomic number (Z) leads to varied electron configurations, different elements each have unique resonant energy edges and edge numbers (Supplementary Fig. 1b). Such an element-specific absorption edge resonance effect implies that combining multiple metals can lead to edge resonance superposition and thus enhanced X-ray shielding performance over a broadened energy window[12].

However, incorporating a large number of metals in a uniform and stable manner, either by alloying or composite engineering, has remained a formidable challenge. Considerable efforts have been devoted to the development of conformable and flexible X-ray shielding materials, which usually involve a polymeric matrix that compromises the shielding performance[8]. To date, Pb-based X-ray shielding materials still

dominate, and the search for high-performance Pb-free flexible alternatives for X-ray radiation protection is far from satisfactory[7,8]. Recently, Ga-based room-temperature liquid metals have emerged as a class of metallic solvent matrices for dispersing elemental metals for improved X-ray attenuation[13,14]. However, with only a limited number of metal species combined, their full potential has yet to be revealed and the trade-off between X-ray shielding performance and material flexibility remains an unresolved limitation.

We hypothesized that a paste-like liquid-metal amalgam (LMA) could serve as a processable metallic host for combining multiple high-Z elements whose absorption edges are distributed across the diagnostic X-ray window. Such edge complementarity should reduce energy intervals of low photoelectric absorption while preserving conformability. To validate this, we selected the room-temperature Ga-In-Sn alloy as the liquid metal matrix for amalgamation-induced metal incorporation and used the energy spectrum of medical X-rays at 100 kVp as the target irradiation condition[15]. While we intended to include the highest possible number of solid metals for maximizing the AER superposition, highly toxic metals (Cd[16], Hg[17], Tl[18], Pb[19]), highly radioactive metals (Tc, Pm, $Z \geq 84$)[20], metals with other safety risks (Sb, Ce, Eu)[21], and those with a low atomic number (Z) and thus low X-ray attenuation coefficients ($Z \leq 44$) were excluded. This resulted in a 27-element LMA consisting of 24 solid metals (namely, Au, Pt, Ir, Os, Re, Rh, W, Pd, Ta, Hf, Lu, Yb, Tm, Bi, Ag, Er, Ho, Dy, Tb, Gd, Sm, Nd, La, Pr) dispersed in the Ga-In-Sn ternary liquid alloy (Supplementary Fig. 1c).

To obtain the optimal formulation for X-ray shielding, we calculated the transmissivity of the LMAs using Monte Carlo simulation to determine the mixing ratios of individual metals[22]. The transmissivity showed a successive decrease as we gradually increased the number of added metal species (Fig. 1b and Supplementary Fig. 2). For the ternary Ga–In–Sn alloy, the optimal weight ratio that gave the lowest transmissivity while maintaining a pure liquid state at room temperature was found to be 50.7% Ga, 29.4% In, and 19.9% Sn by weight. The transmissivity dropped below that of an equivalent-mass 0.5 mm-thick Pb (2.73%) after adding 9 metals, and further reached a transmissivity value as low as 1.51% after introducing all 24 solid metals. The optimized LMA employs a Ga–In–Sn liquid metal matrix (50 vol%, 46.5 wt%) loaded with solid metal species (50 vol%, 53.5 wt%) (Supplementary Table 1).

Mass attenuation coefficient calculations using WINXCOM[23] reveal that the LMA exhibits typical sawtooth structures that correspond to localized resonance energy levels (Fig. 1c). With each having its own characteristic absorption edges, different metallic elements show widely spread resonance energy levels across the 1-100 keV photon energy range. The LMA containing 27 elements features a total of 208 resonance energy levels comprising 27 K edges, 81 L edges, and 100 M edges contributed by all constituent metals (Supplementary Table 2). It should be highlighted that such a high number of resonance energy levels far exceeds that of Pb (9 resonance energy levels including 1 K edge, 3 L edges, and 5 M edges, Supplementary Table 3). The superposition of the 208 absorption edges is expected to create a combinatorial X-ray attenuation effect for wide-range synergistic resonance shielding. The enhanced X-ray shielding (attenuation) by the LMA is evidenced by the substantially reduced photon

transmissivity (< 0.64 relative photon counts) across the 1–100 keV energy range (Fig. 2a). Importantly, LMA, like Pb, shows high mass attenuation coefficients below 40 keV, but demonstrates a substantial advantage in the 40–88 keV range, which is precisely the weak absorption region of Pb, thus providing an effective material design to alleviate the Pb-associated weak absorption in this energy window (Fig. 2b).

From a microscopic mechanistic point of view, the inner-shell core electrons interact with X-rays through the photoelectric effect at resonant energy levels, experiencing a dramatic increase compared to the non-resonant interaction between the outer-shell valence electrons with X-rays (Fig. 1a). According to the Breit–Wigner formula, the resonance effect of an absorption edge is not limited to a single energy level, but is mainly distributed over an energy interval corresponding to the full width at half maximum (FWHM) of the resonance peak (Supplementary Fig. 3)[24,25]. In LMA, the cumulative FWHM intervals from its 208 absorption edges account for 92.1% of the total incident photon distribution (Fig. 2c, Supplementary Table 4). In contrast, the influence range of the absorption edges of Pb accounts for only 2.6% of that total (Supplementary Table 5). Such a stark difference in resonant contribution demonstrates a fundamental shift in the X-ray shielding mechanism of the LMA system, transitioning from a non-resonant-dominated ionization (as in Pb) to a resonant photoelectric effect. Consequently, the resonant-edge superposition of its many metallic constituents, especially the high-Z elements, enables more valence electrons in the LMA to participate in X-ray energy absorption (Fig. 2d), thereby giving rise to a much higher photoelectric effect probability than Pb.

Experimental measurements following the International Electrotechnical Commission Standard 61331-3:2014[26] showed that the transmissivity of the LMA was 1.33% ± 0.04% (Fig. 2e and Supplementary Fig. 4), in good agreement with the calculated result (1.51%). The measured lead equivalent of the LMA was 40% higher than that of pure Pb of the same mass (Fig. 2f)[27]. More importantly, conventional flexible X-ray shielding materials typically employ a limited number of high-Z metallic elements such as Pb, W, Bi, Gd, and Ba fillers for radiation shielding, while a flexible matrix (e.g., polymers) serves as the host material. In these composite systems, the contribution of resonant energy absorption is insignificant, especially since polymeric materials possess intrinsically poor radiation shielding capability. Compared to a polymeric hosting matrix, a liquid metal solvent offers significantly improved X-ray shielding (Supplementary Fig. 5). Consequently, the combination of high shielding effectiveness from multi-element resonant absorption and exceptional flexibility of a liquid metal matrix in the LMA overcomes the trade-off between protective performance and flexibility in conventional X-ray shielding materials. Under 100 kVp tube voltage conditions, the attenuation coefficient of LMA reached 4-100 times higher than that of traditional flexible X-ray shielding materials (Supplementary Table 6, Fig. 2g)[22,28–47]. While increasing the number of filler elements in the LMA leads to more pronounced resonant X-ray absorption, a shielding performance superior to that of Pb is achievable with composition-simplified LMA systems. To validate this, we show that incorporating non-precious metals W and Bi in the Ga-In-Sn liquid metal matrix is able to achieve an improved shielding performance over Pb within a large window of mixing ratio (Supplementary Fig. 6).

The successful preparation of the LMA system is enabled by the strong intermetallic interaction between the Ga-based liquid metal and solid metal particles as well as the oxide-mediated bonding, which permits the incorporation of diversified metallic elements in the liquid metal[48]. The viability of effectively dispersing the 24 metals inside the Ga-In-Sn liquid metal matrix is individually validated (Supplementary Fig. 7, Supplementary Table 7). The resulting LMA, composed of both liquid metal and solid metal particles, exhibits a paste-like state. Rheology tests reveal that the LMA behaves as a shear-thinning fluid (Fig. 3b). Despite the fact that the LMA prepared in this study contains an exceedingly large number of metallic elements, scanning electron microscopy (SEM) and energy-dispersive X-ray spectroscopy (EDS) mapping revealed a uniform distribution of all constituent elements, indicating highly effective element dispersion. X-ray diffraction (XRD) further reveals that the LMA consists of multiple intermetallic phases mixed with the liquid metal phase (Supplementary Fig. 8). Due to the large number of constituent elements and the possibility of greatly diversified intermetallic phases, it is not feasible to accurately assign the XRD peaks.

Given that the environmental and testing conditions can vary substantially under practical shielding applications across medical imaging, aerospace industries, and other fields, the X-ray shielding performance of the LMA was evaluated under application-relevant conditions. For this purpose, LMA layers of different thicknesses were coated onto a supporting styrene-isoprene-styrene (SIS) film (50 μm in thickness). It is found that the samples demonstrated excellent stretchability, reaching a strain of 1000% without mechanical failure (Fig. 3c). Moreover, the 1-cm-thick LMA-SIS composite film maintained > 97% shielding efficiency under 1000% tensile strain (Fig. 3e). When under repeated bending, the shielding efficiency of the 1-mm-thick LMA-SIS composite film remained stable, with a shielding efficiency fluctuation less than 1% (Fig. 3f). We also observed that the samples showed stable shielding performance under temperature variations (Fig. 3g) as well as high-dose irradiation (Fig. 3h). Such excellent stability, crack resistance and self-recovery capability (Supplementary Fig. 9) of the LMA-SIS films are unique features arising from the intrinsic paste-like amalgamation state of the LMA and the complementary resonant edge absorption of its constituent metallic elements. Particularly, the shielding efficiency of the LMA-SIS films is superior to existing X-ray shielding materials over an extended strain range (Fig. 3i).

The X-ray shielding performance of LMA in biological organisms was validated in an experimental model with three groups of C57BL/6 mice, i.e., a blank control group, an 8 Gy X-ray group without X-ray shielding, and an 8 Gy X-ray group using 1 mm LMA as the shielding material. The results demonstrated that the LMA is able to provide excellent protection at the molecular, cellular, tissue, organ and individual levels, compared with the control and the non-shielded group: i) At the molecular level, no radiation-induced DNA double-strand breaks or other damage were observed when X-ray shielding was provided (Fig. 4a). ii) At the cellular level, hematopoietic function of the mice remained normal with LMA shielding (Fig. 4b). iii) At the tissue level, no significant apoptotic signals were observed in the small intestinal mucosa, and the intestinal barrier function remained intact (Supplementary Fig. 10). iv) At the organ level, stable superoxide dismutase (SOD) levels were maintained in the lungs (Fig. 4c). v) At the individual level, the X-ray shielding effectiveness of the LMA was manifested as complete survival with

normal weight gain and development (Fig. 4d). We found that a 1 mm LMA achieves 99% dose attenuation, corresponding to a dose (0.08 Gy) far below the direct damage threshold (0.50 Gy). This means that the LMA not only blocks direct ionizing DNA damage but also reduces indirect damage caused by radiation-induced reactive oxygen species (ROS) through the abrupt dose drop, forming an effective dual-blocking protective mechanism for organisms.

The LMA also demonstrates significant potential in the field of radiation medicine. The LMA can be readily coated onto common gloves and aprons to fabricate X-ray shielding wearables. Independent CT and DSA tests have shown that wearing an LMA glove and an LMA apron provides effective radiation protection (Fig. 4f). In the meantime, the LMA protective suit is 50% lighter than its Pb-based equivalents (Fig. 4e and Supplementary Table 9), which is expected to substantially improve the comfort for patients and medical workers while extending continuous clinical wear fatigue tolerance. Being conveniently applicable, the LMA is also expected to enable easily customizable X-ray shielding wearables and devices in other radiation protection settings.

In summary, this study explored absorption edge resonance for enhancing distribution of energy levels in the LMA X-ray shielding materials. This effect increases the interaction probability between inner-shell electrons and X-ray photons, amplifying the photoelectric effect and leading to synergistically improved radiation shielding. A flexible X-ray shielding material incorporating 27 metallic elements was developed based on this strategy, and the resulting amalgam exhibited superior radiation shielding performance compared to the previously reported X-ray shielding materials under 100 kVp radiation conditions at equivalent mass. Notably, when compared to existing commercial Pb-based X-ray shielding materials, the LMA shielding material demonstrates considerably improved performance measured by radiation protection efficacy, flexible adaptability, weight, mechanical tensile properties, and environmental compatibility. This work establishes a general material design pathway and provides a viable, application-oriented solution for advancing next-generation X-ray shielding materials.

Methods

Preparation of LMA

A total of 27 solid metallic elements were prepared in advance (Supplementary Table 9). Precise amounts of Ga, In, and Sn were weighed according to their mass ratios and placed at the bottom of a quartz crucible (inner diameter: 14.72 mm; height: 70.90 mm). The ingot was melted at 1000°C for 18 h in a high-purity argon atmosphere. The crucible was positioned at the centre of the heating platform inside a vacuum chamber. The chamber was evacuated to 5×10^{-3} Pa and then backfilled with high-purity argon to 0.05 Pa. The sample was melted using the heating platform and subsequently cooled to room temperature within the furnace, yielding the liquid metal solvent.

At room temperature under an oxygen-containing atmosphere, various solid metal powders (Rh, Pd, Ag, Hf, Ta, W, Re, Ir, Pt, Au and Bi) were sequentially placed at the bottom of a polytetrafluoroethylene (PTFE)

mortar. The liquid metal was then poured over the powder surface, and the mixture was ground with a PTFE pestle until all solid particles were fully incorporated into the liquid metal. The resulting composite was subsequently transferred to an argon-filled glovebox. Under oxygen-free conditions at room temperature, additional solid metal powders (La, Pr, Nd, Sm, Gd, Tb, Dy, Ho, Er, Tm, Yb, Lu and Os) were sequentially added to the bottom of a PTFE mortar. The as-prepared liquid metal mixture was again poured onto the powder surface, followed by grinding with a PTFE pestle until complete incorporation of all solid particles was achieved.

X-ray transmissivity simulations

Monte Carlo simulations were performed following the International Electrotechnical Commission (IEC) 61331-1:2014 standard, using a tube voltage of 100 kVp (with a 2-mm-thick Al filter) and 10^9 particle histories to ensure statistical convergence. A 0.5-mm-thick Pb layer (areal density: 0.567 g cm^{-2}) served as the reference for equivalent shielding. Transmissivity was quantified using the mass-energy absorption coefficient ratio relative to air. The liquid metal solvent was modelled as a pure homogeneous liquid phase, whereas composite systems consisting of the liquid metal solvent and solid metal solutes were calculated at a 1:1 volume ratio. Owing to the large number of elements under investigation, a full combinatorial optimisation over all possible elemental combinations would have been computationally prohibitive. Therefore, a sequential strategy was adopted: two solid elements were first selected and optimised as a binary system; the optimised composite was then treated as a single component, with additional solid elements introduced one at a time and reoptimisation performed at each step until all 24 elements had been incorporated.

Simulation of relative photon and electron counts

In the Monte Carlo simulations, the 0–100 keV energy range was divided into 101 intervals, and photon counts at each energy were recorded at the output surface. Because the output count is proportional to the input count, direct comparisons of absolute values are affected by the input intensity. To address this, all recorded counts were normalised by removing the order-of-magnitude factor (10^n) and retaining only the coefficient. The resulting normalised value is defined as the relative photon count, enabling cross-energy comparisons that are independent of input intensity variations.

To evaluate the role of electrons as energy carriers in the shielding material, the deposited electron energy within the material was quantified. Over the 0–100 keV energy range, the photoelectric cross section is much larger than the Compton scattering cross-section; therefore, the deposited electron energy can be reliably attributed to photoelectric interactions. The relative electron count was obtained using the same normalisation procedure.

Calculation of photon energy range for absorption-edge resonance effects

Based on the photoelectric atomic cross section, we defined three key components at each absorption edge. The right-hand limit of the discontinuous cross section function is termed the total photoelectric effect; the left-hand limit is termed the non-resonant photoelectric effect; and the difference between these two limits is defined as the edge-resonant photoelectric effect. According to the Breit–Wigner formula, the resonance width is given by the full width at half maximum (FWHM) of the resonance peak. This FWHM interval was taken as the energy range over which the resonance predominantly influences the absorption process. The incident photon energy distribution was then weighted over this interval, yielding the effective influence range of the absorption edge for both the LMA and Pb.

X-ray transmissivity measurements

The X-ray reference radiation source was based on an industrial X-ray machine equipped with a COMET MXR-320/26 X-ray tube (tungsten target, 20° target angle, 3-mm-thick beryllium inherent filtration), powered by two Gulmay GX160 160 kV, 45 kHz high-frequency generators operated at 100 kVp. The beam was collimated through a primary aperture (1.9 cm diameter, 2 cm thickness) to form a uniform radiation field at the reference plane, with a diameter of 9 cm at 1 m from the focal spot, meeting the requirements for air kerma measurement. A laser positioning system and an ionization chamber support platform were used to facilitate alignment. Under narrow-beam geometry, the attenuation rate was determined from three air kerma rate measurements: one without the test object in the beam; one with a high-attenuation reference block (attenuation factor > 10^5) placed in the beam to account for background and collimator scatter; and one with the test object inserted in the beam. The attenuation rate was then derived as the ratio of the net reduction caused by the test object to the net unobstructed beam intensity.

Preparation of SIS films

SIS (styrene–isoprene–styrene, Kraton 1160) was dissolved at room temperature in a mixed solvent of tetrahydrofuran, N,N-dimethylformamide, and cyclohexane in a weight ratio of 2:1:1. The solution was stirred continuously for 12 h to obtain a homogeneous spinning solution with a concentration of 16.67 wt%. The solution was loaded into a 20-mL syringe and electrospun at an applied voltage of 12 kV, a feed rate of 6 mL h^{-1} and a tip-to-collector distance of approximately 15 cm under a relative humidity of 60 ± 2%. After electrospinning, the SIS film was dried in an oven at 70°C for 8 h and subsequently treated with oxygen plasma.

Rheological characterization

The dynamic rheological properties of the liquid metal paste were systematically characterized using a Haake Mars40 rotational rheometer (Germany) equipped with a parallel-plate measurement system. A

parallel-plate fixture with a diameter of 35 mm was used, with a fixed gap of 1 mm between the plates to ensure uniform shear during testing. All measurements were conducted at a constant temperature of 25°C to eliminate the effects of thermal fluctuations on the viscoelastic behavior. In rotational (steady-shear) mode, the shear rate was incrementally increased from 0.1 s^{-1} to 1000 s^{-1}.

Animal welfare and ethics

All animal experiments were conducted in accordance with the Experimental Animal Welfare and Ethics Review (Approval No. IOZ-IACUC-2025-018) approved by the Experimental Animal Welfare and Ethics Review Committee of the Institute of Zoology, Chinese Academy of Sciences. The study complied with all relevant national and institutional regulations governing the welfare and ethical treatment of laboratory animals.

DNA analysis in bone marrow

Nine male C57BL/6 mice were randomly divided into three groups: (i) blank control; (ii) X-ray irradiation only; and (iii) X-ray irradiation with 1-mm LMA protection. Mice in groups (ii) and (iii) received 8-Gy whole-body X-ray irradiation. Three mice from each group were euthanized on day 7 post-irradiation. Both femurs were harvested, cleared of connective tissue, and the marrow was flushed with 10 mL of 5 mM calcium chloride solution using a 24-gauge needle to prepare a single-cell suspension. DNA was extracted using a Blood/Cell/Tissue Genomic DNA Extraction Kit (DP304-02, Tiangen). Total DNA concentration was measured using a nano-microspectrophotometer.

Bone marrow nucleated cell analysis

Nine male mice were randomly divided into three groups following the same protocol. Three mice per group were sampled on day 7 post-irradiation. Bone marrow single-cell suspensions were prepared as described above and analysed using a fully automated fluorescence cell counter (Countstar Mira FL) to determine total and viable cell concentrations.

Histological and immunofluorescence analysis of intestinal tissue

Nine male mice were randomly divided into three groups following the same protocol. Small intestinal tissue was collected 24 h post-irradiation, fixed in 10% neutral buffered formalin, sectioned, and processed for haematoxylin and eosin (H&E) staining and TUNEL staining.

Superoxide dismutase assay in lung tissue

Nine male mice were randomly divided into three groups following the same protocol. On day 1 post-irradiation, three mice from each group were euthanized, and lung tissue was collected. SOD activity was measured using a total SOD activity assay kit (WST-8 method).

Survival and body weight monitoring

Thirty male mice were randomly divided into three groups following the same protocol. Mice were monitored for survival and body weight over a 30-day period.

Clinical X-ray shielding evaluation

A 0.5-cm-thick layer of LMA was applied to the surface of medical rubber gloves, and the shielded area was imaged using three-dimensional computed tomography (3D-CT) at 100 kVp. Separately, a 1-cm-thick layer of LMA was uniformly coated onto the protective surface of a lead apron, and digital subtraction angiography (DSA) imaging of a human phantom was performed at 96.9 kVp.

Declarations

Data availability

The datasets generated and analyzed in this work are included in this article and Supplementary Information. Further data are available from the corresponding author on request. Source data are provided with this paper.

Acknowledgments

The authors are deeply grateful to Prof. Jinjie Wu and Dr. Rui Zhao from the National Institute of Metrology, China, and Mr. Geng Li from Rad Source Technologies for their assistance in X-ray radiation tests and result analysis; Prof. Guoli Hou from Institute of Zoology, Chinese Academy of Sciences for assistance in the animal experiments; and Mr. Zheng Xiang from HYGEA for their help in the CT and DSA tests.

References

1. Wang S et al (2024) X-ray–induced acoustic computed tomography: 3D X-ray absorption imaging from a single view. Sci Adv 10:eads1584
2. Nicholls RJ et al (2022) Understanding irradiation damage in high-temperature superconductors for fusion reactors using high resolution X-ray absorption spectroscopy. Commun Mater 3:52
3. Sutanto J et al (2026) Radiography in industry: using X-rays and gamma rays for quality control of metals. Int J Adv Sci Eng Inf Technol 16:244
4. Samara ET, Saltybaeva N, Merce MS, Gianolini S, Ith M (2022) Systematic literature review on the benefit of patient protection shielding during medical X-ray imaging: towards a discontinuation of the current practice. Phys Med 94:102–109
5. Tan AWC et al (2026) Advances in elastomeric composites for radiation shielding: a comprehensive review. Int J Smart Nano Mater 17:2679500

6. Wang J et al (2026) Emerging sustainable lead-free X-ray shielding materials: design strategies and future perspectives. ACS Appl Mater Interfaces 18:4590–4610
7. Wu S, Bao J, Gao Y, Hu W, Lu Z (2024) Review on flexible radiation-protective clothing materials. J Mater Sci 59:8109–8133
8. Ihsani RN, Heryanto H, Gareso PL, Tahir D (2024) Innovative radiation shielding: a review natural polymer-based aprons with metal nanoparticle fillers. Polym -Plast Technol Mater 63:738–755
9. Badran HM, Mourad MM, Sharshar T (2026) Effective shielding elements and oxides for medical X-ray applications. Appl Radiat Isot 229:112402
10. Griffiths DJ (2023) Introduction to electrodynamics. Cambridge University Press, Cambridge
11. Bogard JS, Downing DJ, Coleman RL, Eckerman KF, Turner JE (2022) Atoms, Radiation, and Radiation Protection. Wiley, Weinheim
12. Liu Y et al (2025) Fabrication, characterization and optimization design of flexible materials for X-ray shielding with high efficiency. Radiat Phys Chem 226:112265
13. Wang X et al (2025) Non-toxic soft shielding materials for wearable X-ray protection. npj Soft Matter 1:10
14. Wang K et al (2021) Flexible low-melting point radiation shielding materials: soft elastomers with GaInSnPbBi high-entropy alloy inclusions. Macromol Mater Eng 306:2100457
15. Evans DS (1978) Thermal analysis of Ga-In-Sn system. Met Sci 12:411–414
16. Doccioli C, Sera F, Francavilla A, Cupisti A, Biggeri A (2024) Association of cadmium environmental exposure with chronic kidney disease: a systematic review and meta-analysis. Sci Total Environ 906:167165
17. Tepper K et al (2025) Methylmercury demethylation and volatilization by animals expressing microbial enzymes. Nat Commun 16:1117
18. Lennartson A (2015) Toxic thallium. Nat Chem 7:610–610
19. Mitra P, Sharma S, Purohit P, Sharma P (2017) Clinical and molecular aspects of lead toxicity: an update. Crit Rev Clin Lab Sci 54:506–528
20. Schwerdtfeger P, Smits OR, Pyykkö P (2020) The periodic table and the physics that drives it. Nat Rev Chem 4:359–380
21. Ribeiro PG et al (2024) Rare earths as emerging trace element contaminants in the soil. Curr Pollut Rep 10:443–458
22. Wang B et al (2023) A comparative study between pure bismuth/tungsten and the bismuth tungsten oxide for flexible shielding of gamma/X rays. Radiat Phys Chem 208:110906
23. Gerward L, Guilbert N, Jensen KB, Levring H (2004) WinXCom—a program for calculating X-ray attenuation coefficients. Radiat Phys Chem 71:653–654
24. Stöhr J (2023) The nature of X-rays and their interactions with matter. Springer, Cham
25. Henner V, Belozerova T (2022) Analysis of overlapping resonances with unitary Breit–Wigner and K-matrix approaches. Particles 5:451–487

26. Eder H, Schlattl H (2018) IEC 61331-1: a new setup for testing lead free X-ray protective clothing. Phys Med 45:6–11
27. Islam S (2025) MATXCOM—an x-ray/gamma-ray attenuation calculator for arbitrary materials based on EPICS2023 evaluated photon data library. Radiat Phys Chem 229:112433
28. Yılmaz SN, Akbay İK, Özdemir T (2021) A metal-ceramic-rubber composite for hybrid gamma and neutron radiation shielding. Radiat Phys Chem 180:109316
29. Yılmaz SN, Güngör A, Özdemir T (2020) The investigations of mechanical, thermal and rheological properties of polydimethylsiloxane/bismuth(III) oxide composite for X/gamma ray shielding. Radiat Phys Chem 170:108649
30. Özdemir T, Yılmaz SN (2018) Mixed radiation shielding via 3–layered polydimethylsiloxane rubber composite containing hexagonal boron nitride, boron(III) oxide, bismuth(III) oxide for each layer. Radiat Phys Chem 152:17–22
31. GILYS L (2023) Development and investigation of lead-free radiation protection elements providing effective absorption of ionising radiation. Kaunas University of Technology, Kaunas, Lithuania
32. Wu J-K et al (2023) Gd^{3+} ionic nano-aggregate clusters enable metallopolymers redox electrolytes as high-performance flexible radiation shielding. Compos Sci Technol 231:109817
33. Yu L, Yap PL, Santos A, Tran D, Losic D (2021) Lightweight bismuth titanate ($Bi_4Ti_3O_{12}$) nanoparticle–epoxy composite for advanced lead–free X–ray radiation shielding. ACS Appl Nano Mater 4:7471–7478
34. CACIK F (2022) Production of X–ray protection material using electrospinning device and nanomaterial. Necmettin Erbakan University, Institute of Science, Konya, Turkey
35. Asari Shik N, Gholamzadeh L (2018) X-ray shielding performance of the EPVC composites with micro- or nanoparticles of WO_3, PbO or Bi_2O_3. Appl Radiat Isot 139:61–65
36. Poltabtim W et al (2021) X–ray shielding, mechanical, physical, and water absorption properties of wood/PVC composites containing bismuth oxide. Polymers 13:2212
37. Bijanu A et al (2023) Flexible, chemically bonded Bi-PVA–PVP composite for enhanced diagnostic X-ray shielding applications. J Inorg Organomet Polym Mater 33:2279–2291
38. Koyuncu B, Aral N, Candan C, Nergis B (2024) Bismuth oxide nanoparticles/waterborne polyurethane-coated fabrics for ionizing radiation protection. J Coat Technol Res 21:969–978
39. Xu X et al (2025) Study of construction of innovative barite/waterborne polyurethane/low–density polyethylene composites for enhanced X–ray shielding performance. Polymers 17:451
40. Thumwong A et al (2022) A comparative study on X-ray shielding and mechanical properties of natural rubber latex nanocomposites containing Bi_2O_3 or $BaSO_4$: experimental and numerical determination. Polymers 14:3654
41. Poltabtim W et al (2022) Dual X-ray-and neutron-shielding properties of Gd_2O_3/NR composites with autonomous self-healing capabilities. Polymers 14:4481

42. Liu W et al (2024) Flexible lightweight Bi_2O_3-rubber based materials for X-ray protection. Radiat Phys Chem 216:111395
43. Lim-aroon P, Wimolmala E, Sombatsompop N, Saenboonruang K (2019) Manufacturing process and properties of lead-free natural rubber sponge for use in X-ray and gamma ray shielding applications. IOP Conf Ser Mater Sci Eng 526:012015
44. Toyen D, Wimolmala E, Saenboonruang K (2023) Multi-layered composites of natural rubber (NR) and bismuth oxide (Bi_2O_3) with enhanced X-ray shielding and mechanical properties. Polymers 15:2717
45. Thumwong A, Wimolmala E, Markpin T, Sombatsompop N, Saenboonruang K (2021) Enhanced X-ray shielding properties of NRL gloves with nano-Bi_2O_3 and their mechanical properties under aging conditions. Radiat Phys Chem 186:109530
46. Monzen H, Kanno I, Fujimoto T, Hiraoka M (2017) Estimation of the shielding ability of a tungsten functional paper for diagnostic x-rays and gamma rays. J Appl Clin Med Phys 18:325–329
47. La LBT et al (2016) X-ray protection, surface chemistry and rheology of ball-milled submicron Gd_2O_3 aqueous suspension. Colloids Surf A 501:75–82
48. Wang D et al (2023) Liquid metal combinatorics toward materials discovery. Adv Mater 35:2303533

Figures

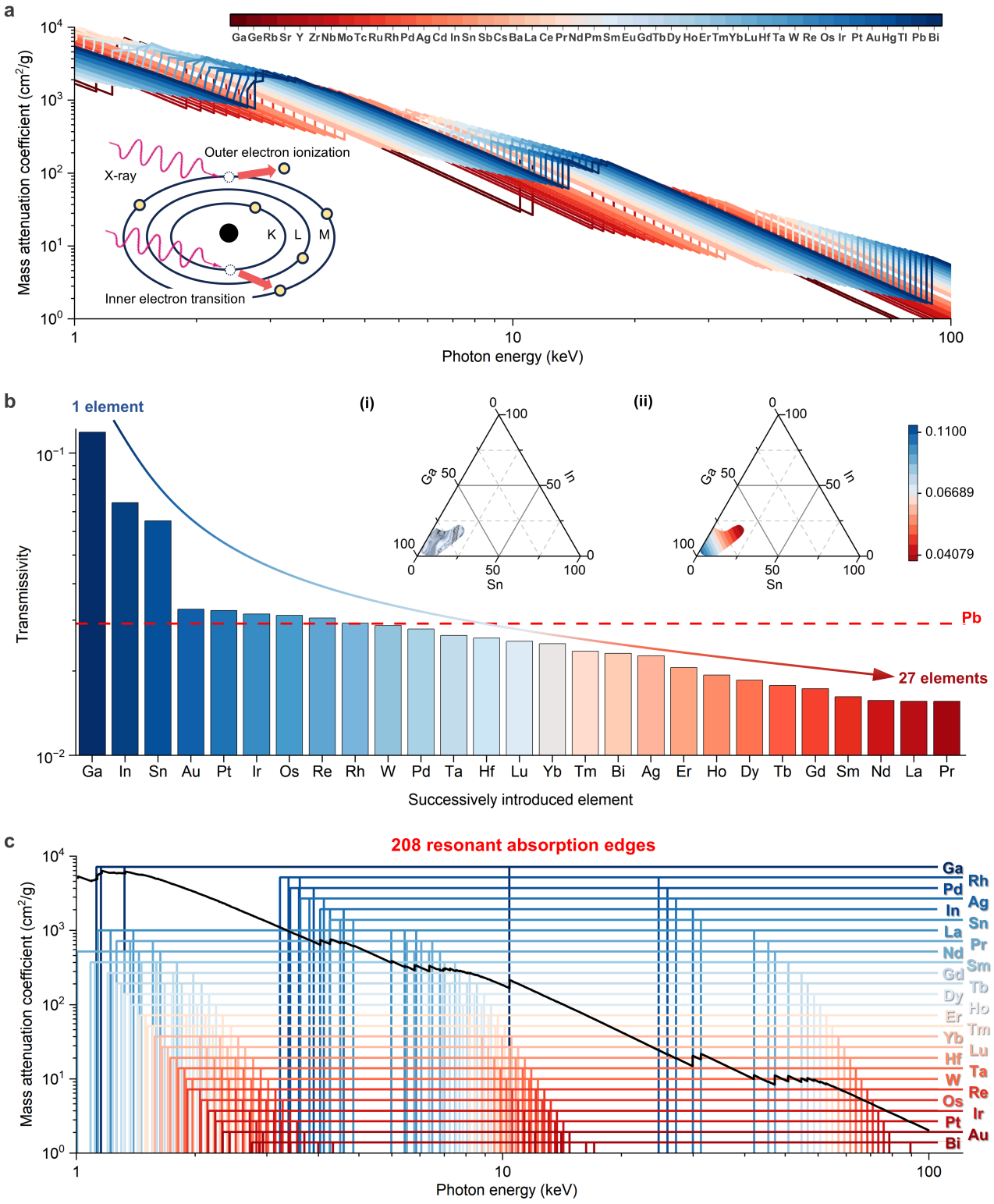


Figure 1

Absorption edge resonance superposition of Ga-based LMAs. a, Mass attenuation coefficients of metallic elements involved in this study. The sawtooth structures in these metals correspond to their characteristic absorption edge resonance. Inset figure: schematics showing the non-resonant ionization of outer-shell electrons and the resonant edge absorption of inner-shell electrons of an element interacting with an X-ray. **b**, X-ray transmissivity of the LMA versus successively increased number of

constituent elements. Inset figure: i) Phase diagram of the ternary Ga-In-Sn alloy. The region enclosed by the liquidus line corresponds to the composition range for stable liquid phases at room temperature (25 °C). ii) X-ray transmissivity distribution in a logarithmic scale. **c**, Mass attenuation coefficient of the LMA in the 1-100 keV photon energy range. The colored lines indicate resonant absorption edges of different metallic elements as indicated, totaling 208 resonant edges.

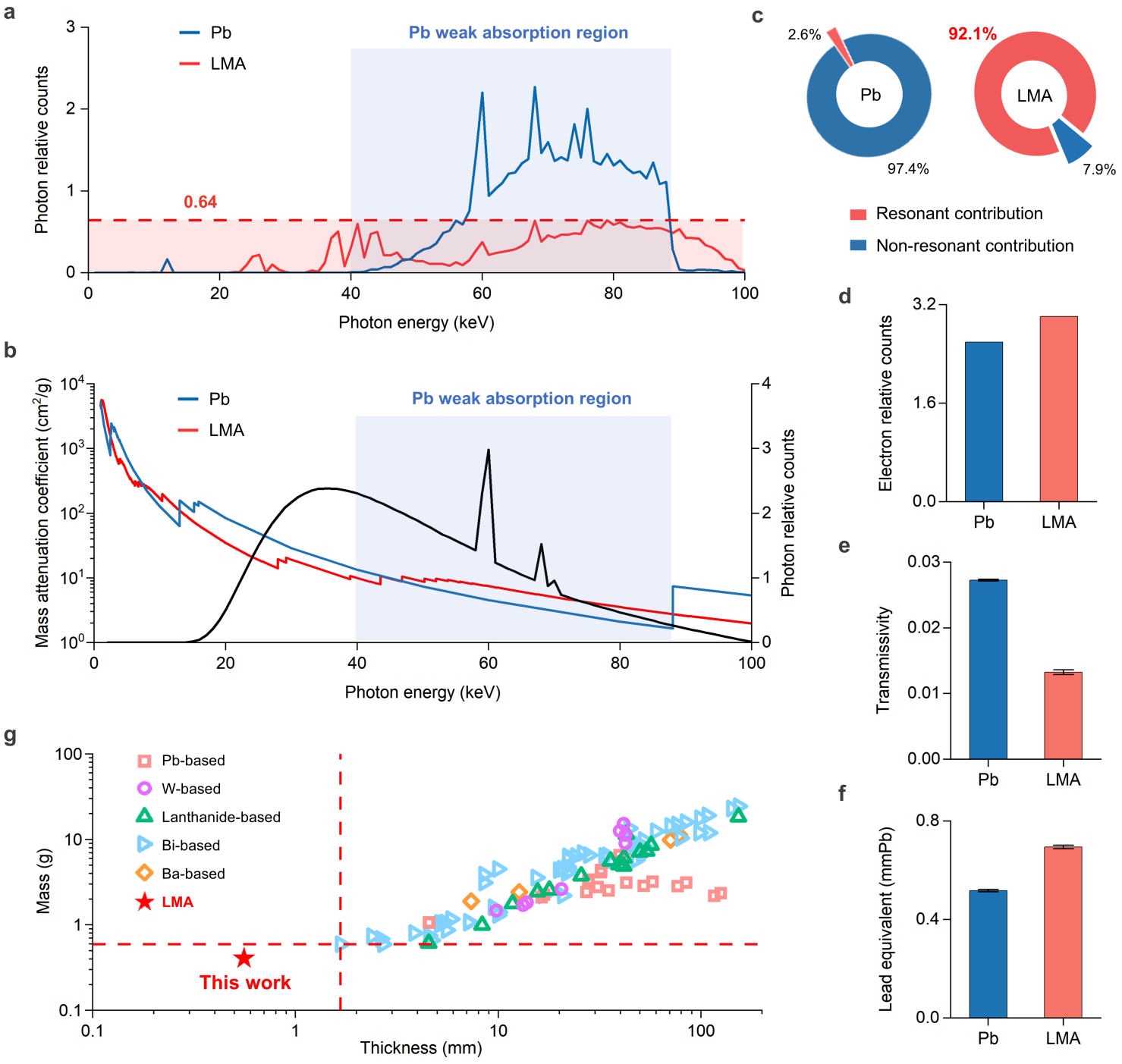


Figure 2

Characterization of material properties and X-ray shielding performance of LMA. a, Output surface photon counts, which represent the relative counts of transmitted X-ray photons penetrate through the

shielding material. **b**, Comparison of the mass attenuation coefficients of LMA and Pb within the photon energy range of 1-100 keV and the X-ray energy spectrum at 100 kVp tube voltage for the reference radiation aluminum (Al) filter recommended by IEC 61331-2014. **c**, Resonant versus non-resonant contributions to the total incident photon distribution for LMA and Pb. **d**, The relative counts of photoelectrons from the shield materials as a result of their interaction with the X-ray. **e-f**, Comparison of experimentally measured X-ray transmissivity (**e**) between 0.5-mm-thick Pb and LMA of the same mass per area, and the corresponding equivalent thickness (**f**). **g**, Comparison of mass and thickness required for different X-ray shielding materials to achieve comparable X-ray shielding performance equivalent to that of 0.5 mm Pb per unit area (1 cm^2).

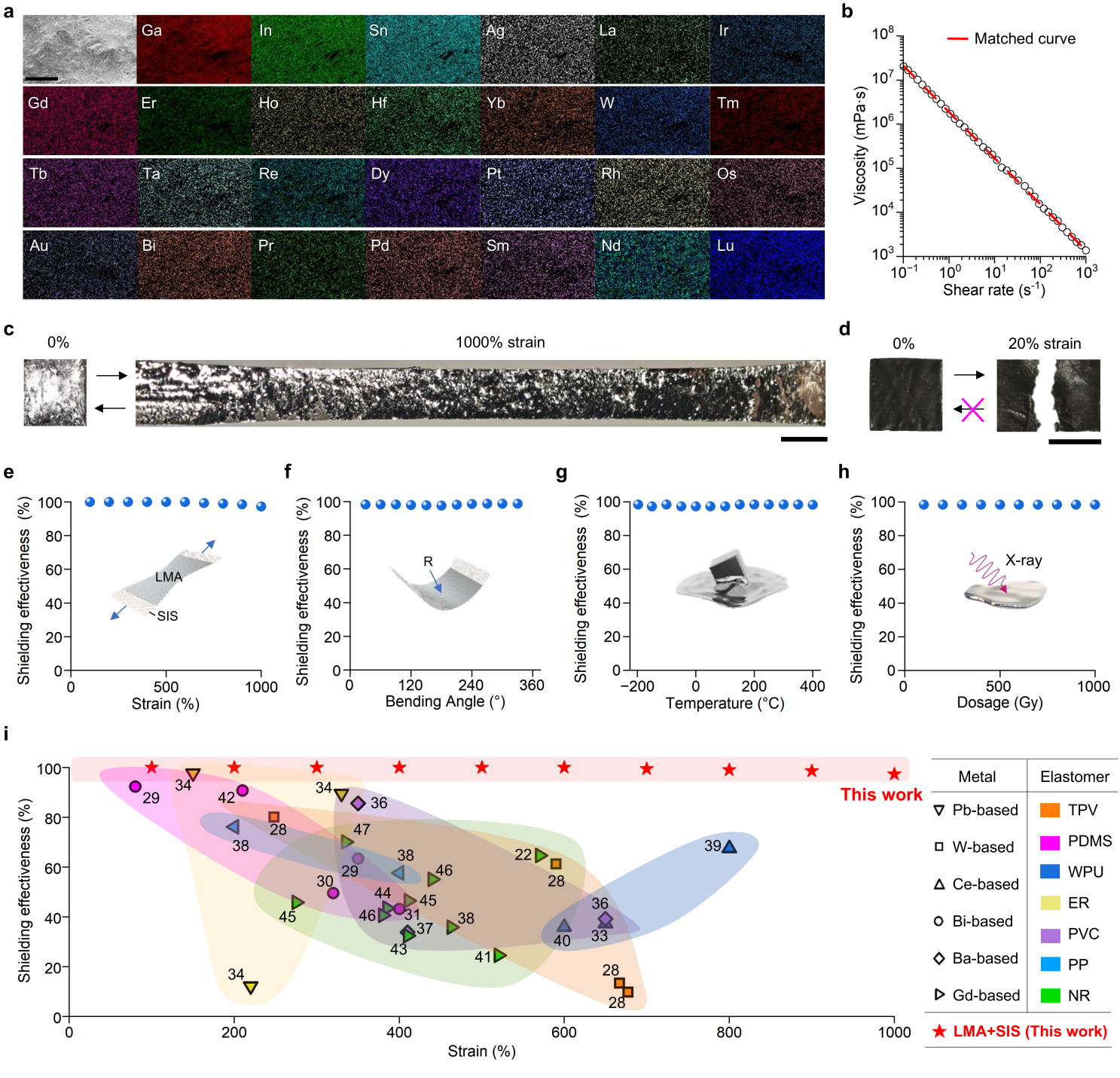


Figure 3

LMA for stretchable and crack-resistant X-ray shielding. a, SEM and EDS elemental mapping of the LMA containing 27 metallic elements. Scale bar: 500 μm. **b**, The rheological behaviour of the LMA. **c**, Reversible stretch and release of an LMA-SIS film. Scale bar: 1 cm. **d**, Reversible stretch and release of a Pd foil which cracks during tensile testing. Scale bar: 1 cm. **e**-**h**, X-ray shielding effectiveness of the LMA-SIS composite films under (**e**) uniaxial strain (1 cm in total thickness); (**f**) bending (curvature radius: 0.2 m); (**g**) temperature variations, and (**h**) long-term irradiation (**f**-**h**, 1 mm in total thickness) (**e-h**, values are averages of triplicate measurements). **i**, Comparison of the shielding efficiency of different material systems within 1000% strain range. The shielding effectiveness based on 1 cm material thickness is considered and compared (ER: epoxy resin; NR: natural rubber; PDMS: silicone rubber; PP: polyvinyl alcohol and polyvinylpyrrolidone; PVC: polyvinyl chloride; TPV: thermoplastic vulcanizate; WPU: waterborne polyurethane).

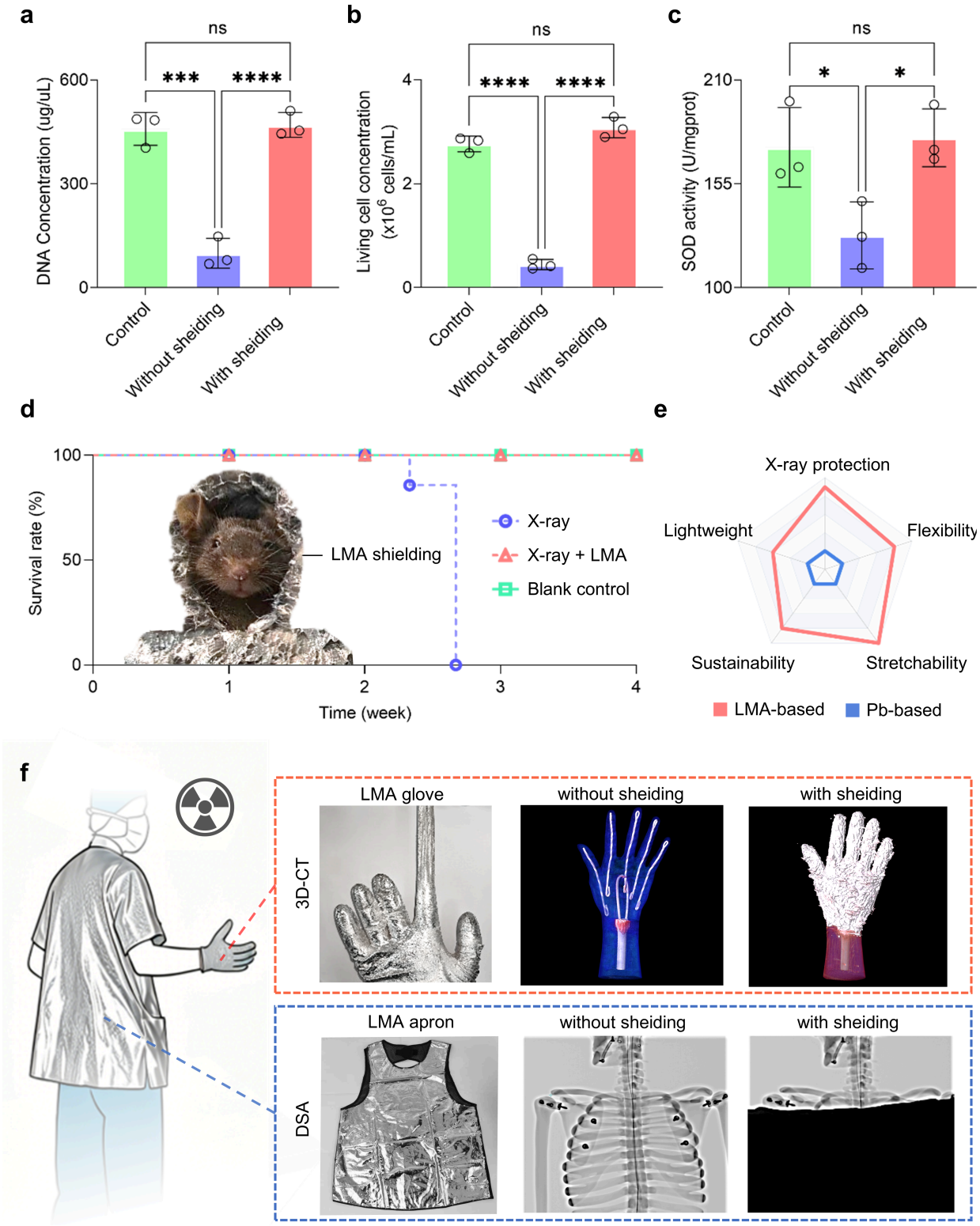


Figure 4

Demonstration of the LMA shielding performance in medical X-ray protection. a-c, Comparison of molecular, cellular, tissue-level X-ray shielding performance in a control, non-shielded and LMA-shielded group: (**a**) DNA concentration in bone marrow, (**b**) living cell concentration in bone marrow, and (**c**) SOD activity in mouse lungs. **d**, Survival rate of C57BL/6 mice over time following high-dose X-ray irradiation for a control, non-shielded and LMA-shielded group. Inset figure: A C57BL/6 mouse wearing an LMA-

based X-ray shielding suit. **e**, Comparison of Pb-free LMA and commercial Pb-based X-ray shielding materials based on five metrics: X-ray shielding performance, flexibility, stretchability, weight and sustainability (Pb content). **f**, LMA X-ray protection sets for different body parts (3D-CT: three-dimensional computed tomography; DSA: digital subtraction angiography).

Supplementary Files

This is a list of supplementary files associated with this preprint. Click to download.

- SupplementaryMaterials.docx